

# Hybrid Nanocrystalline Ribbon Core and Flake Ribbon for High-Power Inductive Power Transfer Applications

Yibo Wang, *Student Member, IEEE*, C. Q. Jiang, *Senior Member, IEEE*, Chen Chen, Tianlu Ma, Xinru Li, and Teng Long, *Member, IEEE*

**Abstract**—This paper examines the performance of a 13kW high-power inductive power transfer system utilising a hybrid core structure with novel nanocrystalline ribbon cores and nanocrystalline flake ribbons. Conventional laminated nanocrystalline ribbon cores exhibit excessive edge losses due to high flux density concentrated on the edge and high eddy current losses in the lateral wall, potentially causing partial thermal runaway. To mitigate this issue, the solution is proposed to employ nanocrystalline flake ribbons as a shielding material on the edge while maintaining the nanocrystalline ribbon core as the main magnetic coupler. The performance of the hybrid core is evaluated under different power levels up to 13.8 kW. Experimental results reveal a nearly 2% increase in peak efficiency compared to the ferrite DMR44 and a 1% increase compared to standalone nanocrystalline ribbon cores, bringing the peak DC-DC efficiency to over 96%. Moreover, under 6.6 kW output power, the temperature rise after 2-hour operation is significantly reduced to a maximum temperature of 76.5 °C with the proposed hybrid core, compared to 96.4 °C with the ferrite shield and 110.6 °C without any edge shield. The design highlights using nanocrystalline material in inductive power transfer systems to improve efficiency and thermal performance.

**Index Terms**—Inductive power transfer (IPT), nanocrystalline core, flake ribbon, magnetics design.

## I. INTRODUCTION

INDUCTIVE power transfer (IPT) systems, a form of wireless power transfer (WPT) technology, enable high power energy conversion without the need for heavily insulated cables and high maintenance costs [1], [2]. As the global shift towards vehicle electrification, including industrial vehicles, automated guided vehicles, public road vehicles and so on, the demand for improving IPT technologies grows more urgent. This includes a focus on increased reliability, high power output, and high power density [3], [4].

The main hurdle in achieving these goals mainly stems from the magnetic materials employed in IPT systems, which is an essential component to realise high power output [5]–[7]. At present, MnZn ferrites are widely used due to their easy availability, cost-effectiveness, and relatively decent magnetic properties [8]–[10]. However, with the growing demand for power density, intrinsic properties of MnZn ferrites like low saturation flux density, low thermal conductivity, and low thermal stability present challenges for IPT development. Furthermore, MnZn core losses make up a considerable part of

the total loss in IPT, limiting the maximum efficiency. Consequently, addressing these issues is crucial for the future development of wireless charging technology.

In recent years, numerous studies have investigated alternatives to MnZn ferrites in order to find a suitable replacement. Nanocrystalline materials, in particular, have attracted growing attention for IPT applications, as they offer greater flexibility in core design and exhibit superior magnetic properties compared to ferrites [11], [12]. In [13], the feasibility of using the laminated nanocrystalline ribbon core (NRC) in IPT was thoroughly studied. Performance was compared with MnZn ferrites. Although the nanocrystalline ribbon core exhibited better performance in terms of coupling factor, curie temperature, and permeability. Its efficiency was 2% lower than that of ferrite due to high eddy current losses. Design recommendations for accommodating the unique characteristics of nanocrystalline ribbon cores have been proposed in [14]. The proposed structure with nanocrystalline ribbon cores eliminates the gap between the core bars, resulting in increased efficiency and reduced temperature levels. However, the edge current loss effect was not clearly explained, and corresponding countermeasures have not been applied. [15] and [16] introduces the gap losses in transformer and inductor of laminated cores which are the similar phenomenon of the edge loss in IPT. However, the proposed model assumes a uniform direction of the main flux and a controllable air gap, which does not apply to IPT applications where the leakage flux dominates. In [17], rectangular windings were utilized for the NRC to minimize uneven edge losses. Nonetheless, the winding size was excessively large, resulting in a low power density, which diminishes its effectiveness in practical applications, especially in the field of automotive wireless charging. Another type of nanocrystalline material newly emerged, nanocrystalline flake ribbon (NFR), was utilised in inductor design in [18]. This material offers greater flexibility, as adjusting the ratio of polyester film to nanocrystalline ribbon enables tuning of permeability and conductivity. This capability can also be extended to IPT designs. Overall, prior studies have demonstrated the significant potential of nanocrystalline materials in IPT. However, issues such as eddy current loss and excessive edge temperature rises were not thoroughly examined and analysed. This paper delves deeper into core structure design using hybrid NRC and NFR to enhance efficiency and thermal dependability in IPT systems.

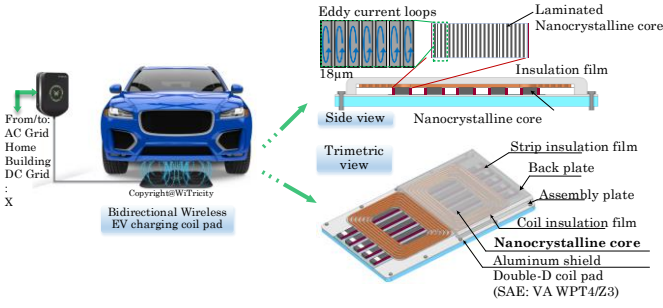


Fig. 1. Magnetic core configuration with a double-D coil pad and Nanocrystalline ribbon core. The coil pad is compatible with the class of WPT4 (22 kVA) Z3 (170-250 mm) in SAE J2954.

Section II presents the mathematical model and equivalent circuits for series-series (S-S) compensated IPT. Circulating energy analysis is mathematically explained which is used later in the experimental verification, providing a more straightforward evaluation process for the magnetics. Section III elaborates on the properties of NRC and NFR, and the mechanism of edge loss in the laminated core is explained using equivalent magnetic circuits. Section IV introduces countermeasures involving NFR shielding and provides simulation results comparison. In Section V, experimental validation is carried out by constructing a high-power IPT prototype based on simulation parameters and measuring efficiency across various input voltages and output power levels. The results reveal improved performance with NFR shielding, and extended temperature tests demonstrate enhanced thermal stability with the proposed core structure.

## II. ANALYSIS OF SERIES-SERIES COMPENSATED IPT AND CIRCULATING ENERGY ANALYSIS

### A. S-S compensated IPT with nanocrystalline core

Fig. 1 shows the proposed concept of automotive inductive power transfer utilizing nanocrystalline material as magnetic couplers. The ground assembly (GA) connected with the charging box which connected then with the grid input. Vehicle assembly (VA) connected with the rectifier on the vehicle and charging the battery with DC current. The VA and GA consist of winding coils, magnetic cores, and aluminium shield. Laminated NRCs are placed along the flux pipe direction, resulting in a reduced eddy current loop. Sided magnetic shields are added for countering the edge effect of the NRC, which will be explained in detail in the following sections.

Nowadays, with the help of wide band gap semiconductors, the converters have achieved remarkable efficiency levels up to 99% [19]. The inherent resonant structure of IPT make soft-switching easy to realise. The primary obstacle in attaining optimal efficiency for IPT systems lies in the coupler pads, particularly the magnetic materials.

Various topologies can be employed to adjust the coupler pad for attaining magnetic resonance [20]. Among these, the series-series compensation method is deemed effective and convenient for battery charging applications. This topology provides a constant current output, ensuring a steady charging current irrespective of battery voltage, which in turn results in

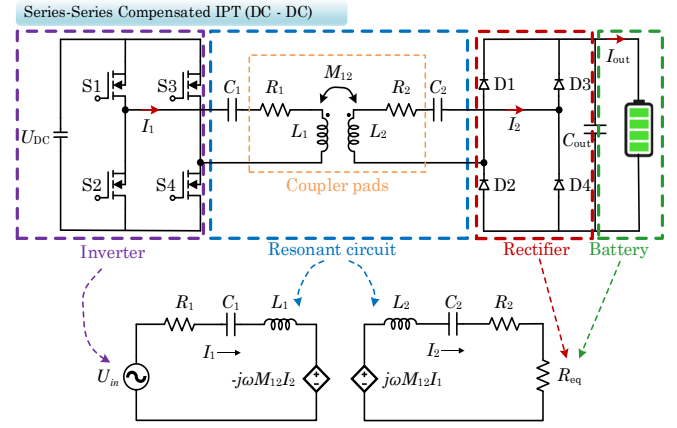


Fig. 2. Most commonly used S-S compensated IPT and the equivalent circuits to verify the proposed hybrid nanocrystalline core design.

enhanced interoperability.

A typical schematic of S-S is shown in Fig. 2, the full bridge inverter (S1-S4), converts the DC input voltage to square wave and excites the resonant circuits. Primary current  $I_1$  becomes nearly sinusoidal as the combination of LC results in a high quality factor. The secondary side can use full bridge passive rectification (D1-D4) for simplicity. With output capacitor  $C_{out}$  filtering current harmonics, a constant charging current  $I_{out}$  can feed to the load.

The coupler pads can be modelled as coupled inductors. In the equivalent circuit,  $\omega$  is the switching frequency in radian.  $R_1$  and  $R_2$  are the sum of winding resistances and ESR of the compensation capacitors  $C_1$  and  $C_2$ , while  $L_1$  and  $L_2$  are the inductances of the primary and secondary windings respectively. The mutual inductance  $M_{12}$  describes the coupling between primary and secondary pads. The primary and secondary circuits can then be modelled separately with current control voltage sources (CCVS), where  $-j\omega M_{12}I_2$  on the primary circuit and  $j\omega M_{12}I_1$  on the secondary circuit. The rectifier and battery load can be equivalent to a resistive load  $R_{eq}$ . The equivalent impedances of primary  $Z_1$  and secondary side  $Z_2$  can be calculated as,

$$\begin{cases} Z_1 = R_1 + j\omega L_1 + \frac{1}{j\omega C_1} \\ Z_2 = R_2 + j\omega L_2 + \frac{1}{j\omega C_2} \end{cases} \quad (1)$$

According to Kirchhoff's law,

$$\begin{cases} Z_1 I_1 - j\omega M_{12} I_2 - U_{in} = 0 \\ j\omega M_{12} I_1 - Z_2 I_2 - R_{eq} I_2 = 0 \end{cases} \quad (2)$$

Assuming the passive parameters of primary and secondary are symmetric. When the system operates in a resonance frequency of  $L_1$  and  $C_1$ , the impedance of the resonant tank on each side is effectively cancelled. Combining the equations in (1) and (2), the reflected impedance  $Z_{ref}$ , primary current  $I_1$  and output power  $P_{out}$  can be calculated as (3).

$$Z_{ref} = \frac{\omega^2 M_{12}^2}{R_{eq}}, I_1 = \frac{U_{in}}{R_1 + Z_{ref}}, P_{out} = \frac{U_{in}^2 R_{eq}}{\omega^2 M_{12}^2} \quad (3)$$

This indicates that the output power is directly controlled by  $U_{in}$ . The maximum efficiency  $\eta_{max}$  can be deduced in (4) [21].  $Q_1$  and  $Q_2$  are the quality factor of the primary and secondary side respectively.  $k$  is the coupling coefficient which can be calculated as  $k = M_{12}/\sqrt{L_1 L_2}$ .

$$\eta_{max} = \frac{1}{1 + \frac{2}{k\sqrt{Q_1 Q_2}}} \quad (4)$$

This equation illustrates that as the coupling coefficient and quality factors increase, the maximum possible efficiency is also increased, indicating them as critical determinants for designing IPT systems.

### B. Circulating energy analysis

In assessing magnetic cores, circulating energy analysis is employed in this paper to minimize the effort for hardware testing. With this approach, DC inputs and outputs are directly connected, allowing high power to circulate within the system while draw a low power from the outside source. Consequently, the output current is directly fed back to the input, streamlining the evaluation process. Based on the previous equations, the current and output power can be recalculated with the condition of the primary and secondary voltage  $U_2 = jU_{in}$ . The following equations can be derived,

$$\begin{cases} I_1 = \frac{U_{in}(Z_2 + \omega M_{12})}{Z_1 Z_2 + \omega^2 M_{12}^2} \\ I_2 = \frac{jU_{in}(\omega M_{12} - Z_1)}{Z_1 Z_2 + \omega^2 M_{12}^2} \end{cases} \quad (5)$$

With the switching in resonant frequency, the equivalent load and output power are,

$$\begin{cases} R_{eq} = \frac{jU_{in}}{I_2} = \frac{Z_1 Z_2 + \omega^2 M_{12}^2}{\omega M_{12} - Z_1} \\ P_{out} = jU_{in} I_2^* = \frac{U_{in}^2 (\omega M_{12} - Z_1)}{Z_1 Z_2 + \omega^2 M_{12}^2} \end{cases} \quad (6)$$

Since there is no physical load, the injected power  $P_{inject}$  from the DC source is exactly the entire system loss, which consists of power electronics loss  $P_{ele}$ , winding resistance and capacitor resistive losses  $P_{re}$ , diode conduction losses  $P_{diode}$ , and magnetic material loss  $P_{mag}$ . With the output bulk capacitor  $C_{out}$ , the output current  $I_{DC}$  become DC and feed back to the input. The DC-DC efficiency of the circulating energy system can then be calculated as,

$$\begin{aligned} \eta_{DC-DC} &= \frac{P_{out}}{P_{out} + P_{ele} + P_{re} + P_{diode} + P_{mag}} \\ &= \frac{U_{DC} I_{out}}{P_{inject} + U_{DC} I_{out}} \end{aligned} \quad (7)$$

Therefore, by measuring  $P_{inject}$ ,  $U_{DC}$ , and  $I_{out}$ , the efficiency can be easily obtained. This method is implemented for the evaluations of the magnetic material in this paper.

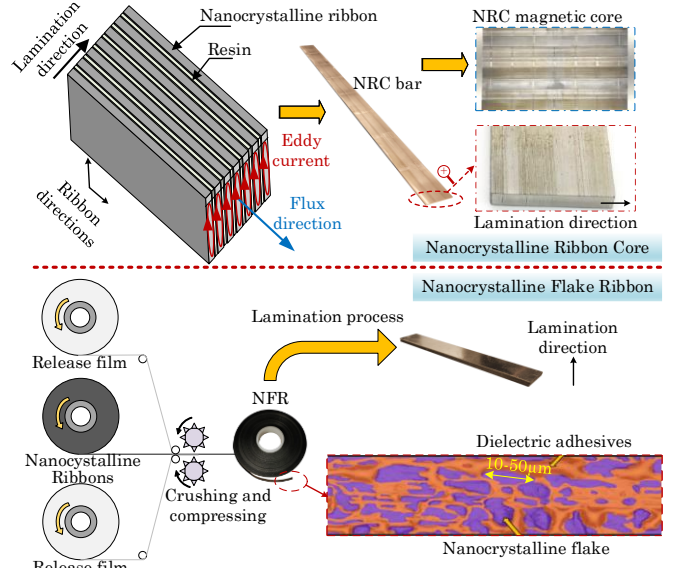


Fig. 3. Configuration of the Nanocrystalline ribbon core and Nanocrystalline flake ribbon.

## III. EDGE LOSS PROBLEM OF NANOCRYSTALLINE RIBBON CORE IN IPT

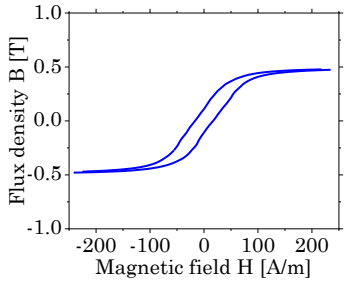
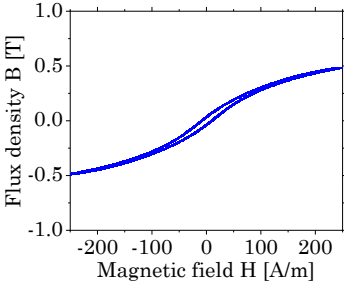
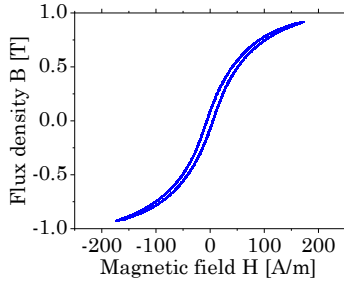
### A. Characteristics of proposed nanocrystalline materials

Nanocrystalline material exhibits high electrical conductivity, leading to considerable eddy current losses when employed as the main magnetic conductor [13]. To tackle this issue, two primary kinds of nanocrystalline cores are implemented. The first is the nanocrystalline ribbon core. The NRC utilizes Fe-Cu-Nb-Si-B based ribbons which are produced by strip cutting the nanocrystalline material. A complete NRC core is then formed by laminating the ribbons with insulating adhesive resin. During the lamination process the resin fills the gap between the ribbons, prevents them from direct contacting and effectively cut the eddy current paths into smaller loops. The ribbon thicknesses typically range from 18 to 20  $\mu\text{m}$ . As depicted in Fig. 3, the effective conductivity is reduced due to lamination, and ultimately the eddy current loss decreases. The stacking factor  $F$  determines the ratio of ribbon to the entire core material. A unity stacking factor  $F = 1$  indicates a solid nanocrystalline core. By changing the stacking factor, permeability and conductivity can be adjusted according to application preferences, the equivalent permeability can be calculated as (8)[14].

$$\begin{cases} \mu_{lamin} = \frac{\mu_r \mu_0}{F + (1-F)\mu_r} \\ \mu_{ribbon} = F \mu_r \mu_0 + (1-F)\mu_0 \end{cases} \quad (8)$$

Here,  $\mu_{lamin}$  and  $\mu_{ribbon}$  are the permeability in lamination and ribbon directions respectively.  $\mu_0$  is the permeability of free space while  $\mu_r$  is the relative permeability of a single ribbon.  $\mu_r \gg \mu_0$ , this also result in  $\mu_{ribbon} \gg \mu_{lamin}$ .

TABLE I PROPERTY COMPARISON OF NRC, NFR AND FERRITE

Property @100kHz, 0.3 T, 25°C	Ferrite DMR44	NFR FN-035	NRC F3BC460425
Rel. permeability $\mu_r$	2400	2300* 2.44**	17710* 4.34**
Lamination factor $F$	N/A	41%	77%
Conductivity $\sigma$	0.05 S/m	12 S/m	$6.41 \times 10^5$ S/m* 21.9 S/m**
Core loss $P_c$	1200 kW/m <sup>3</sup>	506 kW/m <sup>3</sup>	475 kW/m <sup>3</sup>
Eddy current loss $P_e$	47 kW/m <sup>3</sup>	178 kW/m <sup>3</sup>	264 kW/m <sup>3</sup>
Coercive field $H_c$	16 A/m	8.7 A/m	6.3 A/m
Saturation $B_{sat}$	0.45 T	0.49 T	0.947 T
Magnetostriction $\lambda_{sat}$	$-0.6 \times 10^{-6}$	$< 1 \times 10^{-6}$	$< 1 \times 10^{-6}$
Density $\rho$	4800 kg/m <sup>3</sup>	3532 kg/m <sup>3</sup>	5717 kg/m <sup>3</sup>
Max. Temperature	140°C	155°C	155°C
B-H curve*			

\*Ribbon directions. \*\*Laminated directions.

Note<sup>1</sup>: Lamination factor of NFR is excluding single layer flakes.

Note<sup>2</sup>: The saturation flux density of the NFR and NRC ribbons is 1.23 T. In this table,  $B_{sat}$  is re-calculated for a laminated core considering the lamination factor.

The nanocrystalline ribbon core's adaptability enables a high length-width ratio. This is particularly beneficial for inductive power transfer systems. The elongated core bar can span the entire length of the flux pipe without introducing any air gaps, enhancing coupling between the primary and secondary and minimizing leakage flux. However, with the lamination, the NRC obtained anisotropic property which deviates significantly between lamination direction and ribbon direction.

The nanocrystalline flake ribbons are manufactured differently than the NRC, as shown in Fig. 3. The thin nanocrystalline ribbon is compressed alongside with thin release film and then shattered into fine flakes (10-50  $\mu\text{m}$ ), shown in the magnified top view of the flake ribbon. The nanocrystalline flakes and dielectric adhesives are represented by the red and purple areas respectively. This process significantly reduces eddy currents by cutting the current path inside the material. However, the permeability is also reduced due to the introduction of dielectric material within the ribbon. The thickness of the ribbon is about 24 - 30  $\mu\text{m}$ , containing 18 - 20  $\mu\text{m}$  flake ribbons and two sides of 3 - 5  $\mu\text{m}$  adhesive layers. The NFR cores are then made by further lamination of the flake ribbons. Unlike NRC which fills the resin into the ribbons to complete lamination, NFR ribbons can be directly pressed together to form a complete core with the adhesive layer on both sides of the flake ribbons. NFR offers greater flexibility as both ribbons and laminations are adjustable.

Table I shows the property comparison of 3 different types of magnetic core that are used in this research, including NRC F3BC460425 from Hitachi FINEMET, NFR FN-035 from

AT&M, and ferrite DMR44 from DMEGC. The material compositions of the NRC and NFR are both  $\text{Fe}_{73.5}\text{Cu}_1\text{Nb}_3\text{Si}_{15.5}\text{B}_7$ . The lamination factor of NRC and NFR is 77% and 41% (excluding the flakes in single NFR), respectively. The data shown in Table I takes the lamination factor into account and the parameters are measured with laminated core rather than the single ribbon. It is evident that the permeability of NRC in the ribbon direction is substantially higher than the other two materials, exceeding 17,000 in relative permeability, compared to 2,400 for ferrite and 2,300 for NFR. Ferrite has relatively low eddy current loss at 100 kHz. The high coercive field of ferrite indicates most of the core loss comes from the hysteresis loss [22][23]. On the contrary, NRC demonstrates a significantly smaller coercive field but experiences greater eddy current losses, which is less in the case of NFR because of the crushed flakes. The B-H curves for the three materials can support the data. The hysteresis areas of NFR and NRC are narrower than ferrite, implying smaller hysteresis losses. It is worth noting that the eddy current losses of the two nanocrystalline ribbons are calculated based on core loss data using the dynamic core loss model in [24], while the one for ferrite is calculated based on the conductivity using homogenous method [22], [23], [25]. The performance of laminated magnetic core with anisotropic characteristics can deviate greatly in real applications depends on the core geometry, cross-sectional area, and external excitations. The main reason for that is the geometry dependence of the eddy current loss. The core loss data is measured with toroidal cores when the flux direction align with the lamination ribbon direction. In this case,

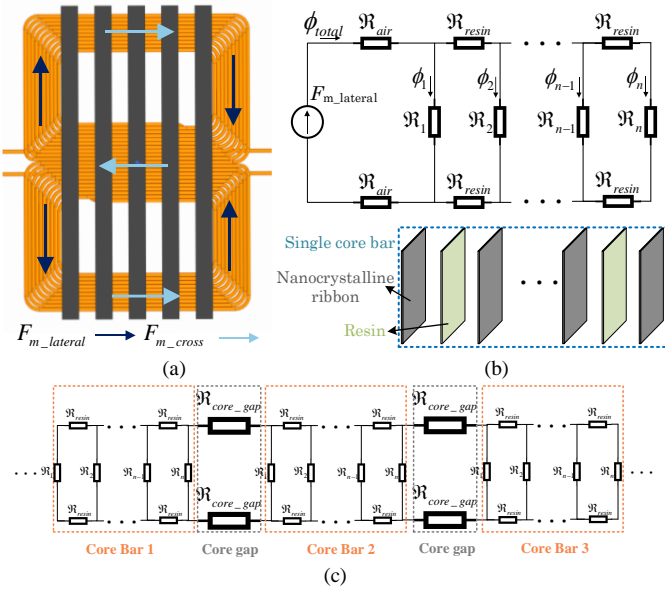


Fig. 4. Intuitive magnetic models in NRC with double D structure. (a) MMF sources. (b) Flux in a single core. (c) Magnetic reluctances in multiple core bars.

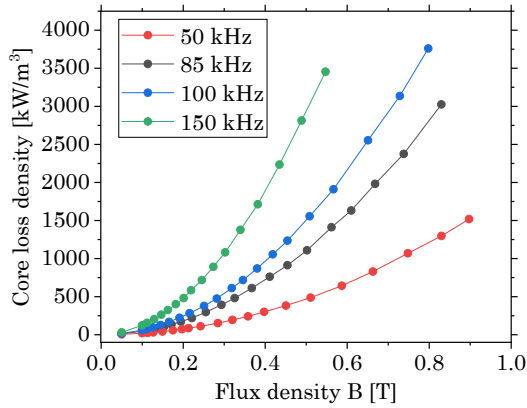


Fig. 5. Core loss data of NRC in 50 kHz, 85 kHz, 100 kHz, and 150 kHz over flux density. The data is imported for FEM simulations.

the eddy current is induced in the cross-section area of the ribbon, which is minimized due to the thin lamination thickness. However, if the magnetic flux enters the ribbon with an angle, the induced eddy current will change due to anisotropic conductivity [26]–[28], leading to the change of the core loss. For inductor and transformer applications where mainstream flux is in parallel with the ribbon direction, the core loss can be calculate by Steinmetz equation based on homogenized flux density [29], [30]. However, for IPT applications, the magnetic flux density distribution is highly uneven due to the dominated leakage flux. Given the core loss dependency on flux density, it becomes essential to address the magnetic flux density distribution within the magnetic material when calculating core loss. In addition, the anisotropic nature of the laminated material requires fine mesh in the core area to obtain a relatively accurate result. Therefore, Finite Element Method (FEM) can be employed to solve the magnetic field within the fundamental tetrahedron inside the region and combine the resultant core loss of each element to determine the total core loss. The FEM results on system

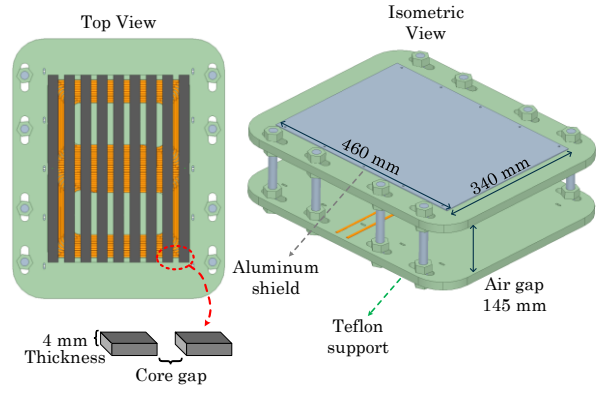


Fig. 6. Top and isometric view of the simulation model of IPT with NRC as magnetic coupler.

parameters like inductance, coupling coefficient and core loss can be used during predesign stage to determine design variables [13], [14], [17], [31]–[33].

Despite experiencing higher eddy current losses, both NFR and NRC exhibit significant reductions in total core loss at the same flux density. It is important to note that the permeabilities of these three materials differ, leading to distinct current excitations when maintaining the same flux density. The nanocrystalline material  $\text{Fe}_{73.5}\text{Cu}_1\text{Nb}_3\text{Si}_{15.5}\text{B}_7$  has saturation flux density of 1.23 T [34]. When considering the stacking factors, the saturation flux densities of NFR and NRC are about 0.49 T and 0.947 T respectively, while the ferrite is about 0.45 T. Both material shows a low magnetostriction at saturation state [35]. Additionally, NRC is the heaviest of the three materials; however, in high-power IPT systems, the increased weight is not a major concern since the magnetic material constitutes a small fraction of the overall weight in high power applications [5]. The maximum operating temperature of NFR and NRC are 155 °C, higher than ferrite at 140 °C.

### B. The edge loss and eddy current effect of NRC.

Although NRC demonstrates its superior characteristic for IPT system and enable much higher power density design than ferrite, the edge effect significantly reduces the stability and reliability of the core. It is the primary reason that the efficiency shows lower than ferrite in [13].

The edge effect is inherently caused by the lamination structure of NRC and the unsymmetric magneto motive forces (MMFs) in double D windings. Due to the complex distribution of leakage and coupling flux, as well as the complicated magnetic path in IPT systems, accurate equivalent circuit is extremely difficult to derive. Nevertheless, in this paper, an intuitive magnetic model is given to explain the edge effect. Fig. 4(a) illustrates a typical double D structure with the arrangement of magnetic cores. Concerning the leakage flux, the MMFs can be simplified based on the current directions into two components: the cross-direction component  $F_{m\_cross}$  and the lateral-direction component  $F_{m\_lateral}$ . The former one cause the flux to primarily follow along the ribbon direction, where eddy currents are minimized due to the small current paths. The latter one generates a significant portion of the flux in the lamination direction, which is perpendicular to the ribbon direction.

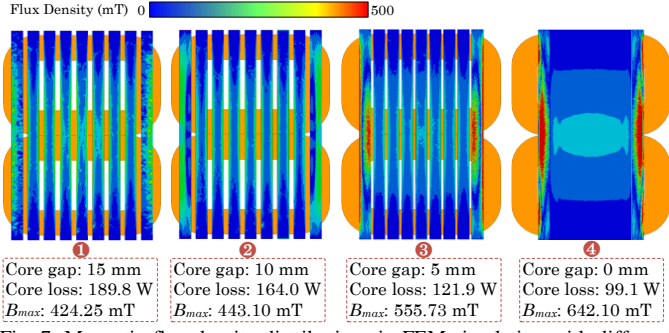


Fig. 7. Magnetic flux density distributions in FEM simulation with different core gaps under 85 kHz frequency.

The intuitive model for a single core is given in Fig. 4(b), where  $\Phi_{total}$  denotes the total flux in the path, total number of nanocrystalline ribbon layers is  $n$ .  $\mathcal{R}_i$  therefore indicates the magnetic reluctance of  $i$ th nanocrystalline layer,  $\mathcal{R}_{air}$  and  $\mathcal{R}_{resin}$  are the magnetic reluctances of air and resin respectively. The magnetic circuit can be intuitively expressed as (9).

$$F_{m\_lateral} = 2 \cdot \phi_{total} \mathcal{R}_{total} + 2 \cdot \sum_{i=1}^n (i-1) \cdot \phi_i \mathcal{R}_{resin} + \sum_{i=1}^n \phi_i \mathcal{R}_i \quad (9)$$

The permeability of resin is considerably lower than that of nanocrystalline material, resulting in a much higher magnetic reluctance for the resin. Therefore, the following relations can be derived.

$$\begin{cases} \mathcal{R}_{air} \gg \mathcal{R}_{resin} \gg \mathcal{R}_i \\ \phi_1 > \phi_2 > \dots > \phi_{n-1} > \phi_n \end{cases} \quad (10)$$

This indicates that the first several dozens of layers carry most of the flux. Combining with the flux excited by  $F_{m\_cross}$  in the cross directions, the centre edge of the core will experience a much stronger flux density compared with other locations of the core. Meanwhile, a considerable part of  $\Phi_{total}$  entering the layers is perpendicular to the ribbon, causing large eddy current on the surface. These two effects will be stronger for outer cores placed near  $F_{m\_lateral}$ . Over time, this non-uniform distribution of flux density and excessive eddy current on the first few layers contribute to unequal losses and temperature increases within the core, reducing thermal stability.

The model can be extended to encompass the entire core structure. As depicted in Fig. 4(c), core gaps further aggravate the edge effect. Each individual core experiences both self edge effect and group edge effects. Since core loss increase exponentially with the increase of flux density, the total loss grows with the introduction of core gaps.

### C. Edge loss simulation with different core gaps

Simulations are then performed to evaluate the edge losses. The core loss data of NRC is shown in Fig. 5. The simulation software breaks the core structure into small tetrahedrons and calculate the corresponding core loss and flux density based on the input data. The simulation result for each tetrahedron is then aggregated to obtain the overall core loss, inductance and coupling coefficient.

Fig. 6 shows the simulation model for the IPT system. The pad dimension is 340 mm  $\times$  460 mm, each pad consists of 9 cores of NRC and the airgap between the primary and secondary pads are

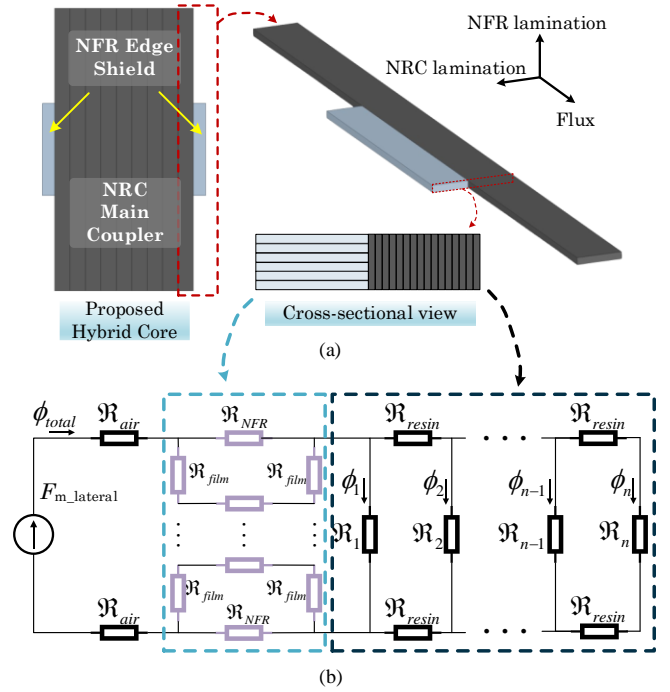


Fig. 8. Proposed hybrid NFR & NRC core structure. (a) Lamination directions for the hybrid materials and cross-sectional view of the cores. (b) Modified intuitive magnetic circuit model with lateral MMF.

145 mm. The thickness of the core is 4 mm, and the width of the core is 25 mm. The length of the core is 460 mm covering the entire length of the winding plane. The core gap is selected as a variable to analyze the edge effect while the thickness and width of the core remain unvaried. Aluminum shields are added to reduce leakage flux. The systems are placed in the Teflon support for further hardware design. This material offers high heat endurance. Simulations are performed under 10 turns, 30 A excitation current in 85 kHz frequency on the primary and secondary double D windings.

Fig. 7 shows the results of core loss and maximum flux density with core gap of 0 mm, 5 mm, 10 mm, and 15 mm respectively. It can be observed that as the core gap increases, core losses also increase from 96.77 W at 0 mm to 200.21 W at 15 mm, resulting in over two times more core loss. However, the edge effect becomes more serious with reduced core gaps. Specifically, at a 0 mm core gap, the flux density in the inner side of the cores is less than 200 mT, while the flux density at the edge of the outer cores exceeds 640 mT. As the core gap increases, the maximum flux density  $B_{max}$  reduces to 424 mT at 15 mm core gap.

Even that both flux densities are still far from the saturation flux density listed in Table I. This exponential difference of flux density in the edge will create uneven loss distribution. These FEM results indicate two crucial insights for NRC core design for IPT. Firstly, eliminating the core gap in core placements is essential to achieve maximum system efficiency. Secondly, the edge effect of NRC causes substantial losses in a small, concentrated area. The large temperature differences substantially raise the likelihood of partial mechanical breakage due to thermal expansion, this effect will be stronger with less core gap, limiting the potential to achieve higher efficiency.

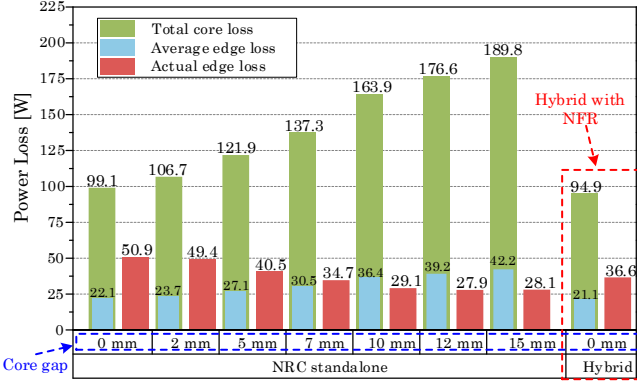


Fig. 9. Core loss comparison of NRC and hybrid NRC & NFR over different core gaps in FEM simulations.

#### IV. PROPOSED HYBRID MAGNETIC CORE STRUCTURE.

##### A. Proposed hybrid NRC and NFR core structure

It is crucial to address the issue of edge loss in order to enhance the reliability of nanocrystalline ribbon cores. Edge shielding can be employed to mitigate eddy currents in the lateral walls and distribute the high flux density concentrated at the edges. By placing an additional magnetic material close to the edge as a shield, the flux density can be effectively dispersed from the nanocrystalline ribbon core. Additionally, the material needs to possess a solid or different lamination structure as the NRC to prevent experiencing similar edge effect. Based on this principle, the following hybrid core structure design is proposed. The core structure is shown in Fig. 8 (a).

- Employ NRC as the primary magnetic coupler to achieve improved coupling factor and self-inductance, taking advantage of its high permeability and low hysteresis losses.
- Eliminate core gaps to achieve higher system efficiency. Core gaps can contribute to uneven flux density among different core bars.
- Utilize NFR as the edge shield of the NRC's lateral walls to reduce the edge effect. The directions of NRC lamination, NFR lamination and main flux pipe are mutually perpendicular with each other. Length of NFR cover only the centre edge of NRC, but not stretching to the flux window, which avoid conducting perpendicular flux to minimise excessive loss introduced by this shield.

The intuitive magnetic model for the hybrid core can then be modified to Fig.8 (b). The introduction of NFR shield can function as a flux divider and transfers a segment of the flux burdened on the NRC edge towards itself. Additionally, the flake ribbon layer, consists of high-permeable nanocrystalline materials, also provides a low magnetic reluctance  $\mathcal{R}_{NFR}$  regionally. Due to different lamination directions between NFR and NRC, the flux entering the lateral wall of NRC can be redirected by the flake ribbons, effectively reducing the eddy current losses on the edge. The dimension of the edge shield should only cover the edge of NRC. This is because the material of edge shield, including both ferrite and NFR, exhibits higher

core loss than NRC. Therefore, the edge shield should not stretch to the flux window and avoid carrying the mainstream flux. In addition, the edge loss effect only concentrates on the centre edge according to the simulation result in Fig. 7, which is the edge area with most winding turns underneath. The geometry of the edge shield should be selected to be effective as well as low-cost. In this research, the dimension of NFR edge shield is designed as 150 mm × 20 mm × 4 mm. The length covers the centre edge, and the thickness is the same with the NRC. The width of the core is selected considering wide commercial availability.

Solid magnetic materials such as ferrite do not possess these features. Also, the permeability of ferrite is significantly lower than that of nanocrystalline materials, which cannot influence the flux distribution near the nanocrystalline ribbons with high permeability.

##### B. Simulation comparison.

By adding the NFR edge shield, the edge effect can be alleviated. For evaluation of the severity of the edge effect. The actual edge loss and average edge loss are defined with (11). The Actual edge loss is the sum of the loss from the four cores placed on the edge, while the average edge loss is four times the average core loss of each core.

$$\begin{cases} \text{Actual Edge Loss} = \sum_{i=1}^4 \iiint_{V_{core_i}} f_{loss_i}(x, y, z) dV \\ \text{Average Edge Loss} = \frac{\text{Total core loss}}{\text{Total core number}} * 4 \end{cases} \quad (11)$$

where  $dV$  indicates the volume of the small tetrahedron used for maxwell equation calculations in the FEM simulations.  $f_{loss_i}(x, y, z)$  is the core loss results distribution function in the  $i$  th edge core, representing the core loss of the tetrahedra at a specific location. The results function is obtained by the FEM simulations.  $V_{core_i}$  indicates the total volume of the  $i$  th edge core. The input of  $f_{loss_i}$  is the location of the core in Cartesian coordinates. By integrating the losses in the core volume of the four cores placed on the edge, the corresponding actual edge loss can be derived. The average edge loss is calculated as four times of the average loss of a single core. By comparing the actual and average edge loss, the distribution of the loss can be deducted. A high difference between the two values indicates a highly concentrated and uneven loss on the edge.

For a core structure exhibiting uniform loss distribution, the actual edge loss should be equal with the average edge loss. Significant discrepancies between these two values suggest a stronger edge effect. In Fig. 9, the simulation results reveal the core losses of the NRC in various core gap scenarios, in comparison to the proposed hybrid core without core gap. It is evident that with an increase in the core gap, there is a significant rise in total core loss, due to the aggregated edge effect for each individual core. The actual edge loss, on the other hand, follows an opposite trend and reaches its highest value of 50.9 W with a 0 mm core gap. This is two times higher than the average edge loss which implies that when NRC is placed without a core gap, more than half of the core loss occurs in the outer cores on both the primary and secondary sides. The edge temperature will

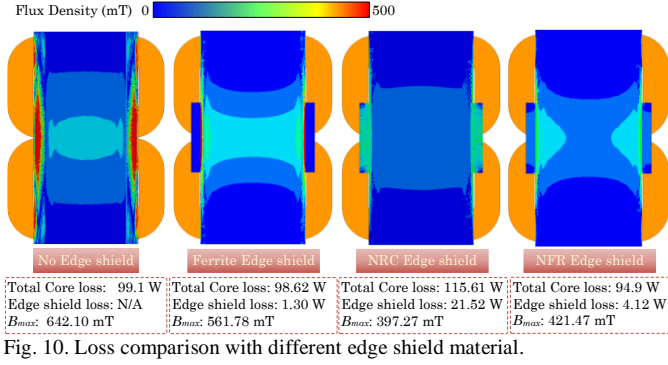


Fig. 10. Loss comparison with different edge shield material.

increase dramatically even the system efficiency is higher. By utilizing the hybrid core, the overall system efficiency is enhanced as the total core loss is reduced by 5 W. More significantly, the actual edge loss is lowered to 36.6 W, which allows for a more evenly distributed loss figure.

### C. Comparison of different hybrid materials.

To demonstrate the advantage of NFR edge shield, simulations with other hybrid materials are performed. The material of the edge shield includes ferrite, NFR, and NRC, and the material of the main coupler is still NRC. Particularly, the edge NRC is laminated with the same direction as NFR when using as the edge shield, which is  $90^\circ$  turn compared with main coupler NRC.

Fig. 10 shows the simulation comparison of the three combinations without core gap. Apparently, after turning  $90^\circ$  and used as edge shield, NRC itself can significantly reduce the flux density concentration on the edge. This is because of its highest permeability compared with other two materials. Ferrite alters the flux distribution pattern of the main NRC core and reduce slightly the core loss. However, as edge shield, it shows very limited capability to alleviate the edge loss effect. NFR can reduce the maximum flux density on the edge to. This is significantly lower than 642.10 mT without edge shield and 561.78 mT with ferrite edge shield.

Nevertheless, when considering the edge shield loss brought by the newly introduced material, NRC edge shield become unacceptable because of extremely high eddy current loss and resulted low efficiency. The four newly introduced NRC edge shields bring over 20 W on the shields and increase the total core loss to 115.61 W. This high energy density on the shields will lead to an exponential temperature increase, resulting from the high conductivity of the nanocrystalline material placing directly on the excitations. NFR edge shield obtains a much promising loss compared with NRC, as the ribbon is crushed to flakes and then reduces the eddy current loss. The simulation results have demonstrated the feasibility and superiority of NFR edge shielding.

### D. Validation of edge shield length.

To verify the proposed dimensions for the edge shield, FEM simulations with parameter sweeping are performed. Since the width and stacking factor of NFR are predetermined by the manufacturing process, the edge shield length is selected as the sweeping variable with a 10 mm step. The results are presented

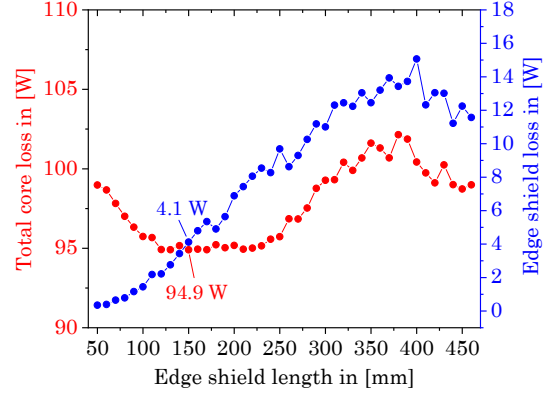


Fig. 11. Total core loss and edge shield loss in different edge shield lengths from 50 mm to 460 mm, with 10 mm step.

in Fig. 11. It is evident that the core loss is relatively optimized in the range of in the length between 120 - 230 mm. Specifically, the core loss is minimized at 150 mm edge shield length. Reducing the length below this 120 mm leads to an apparent decrease in the shielding effectiveness, resulting in higher edge losses. Conversely, edge shields longer than 230 mm exhibit high shield losses. This can be attributed to the higher core loss of NFR compared to NRC. Therefore, the FEM simulations provide validation for the proposed dimension.

## V. EXPERIMENT VERIFICATIONS

### A. Experiment setup

The experiment platform is constructed to demonstrate the proposed hybrid core structure with other magnetic materials, shown in Fig. 11. SiC module CCB021M12FM3 is designed as the full bridge AC inverter; Schottky diode C4D40120D is used for the passive rectifier; BSL800-10 supplies DC power up to 800 V; Tektronix MSO46 with probes THDP0200 and TCP0030A is used to observe current and voltage waveforms, it is also embedded with power suite SUP4-PS2; data logger LR8450 with K-type thermocouples is used for fast temperature data recording; FLIR E6-XT is used to capture the thermal distribution. The test setup is designed with a circulating current loop configuration, where the rectifier output and inverter input are directly connected to process high power operation, allows the circulation of high power within the system while the external power demand remains significantly lower. The power needed from outside is only for system losses and can be used directly to calculate DC-DC efficiency according to (7).

### B. Core structures

Fig. 12 shows the coil structure with the hybrid NRC (edge shield using ferrite or NFR), standalone NRC and ferrite DMR44 for comparison experiments. The NRC core consists of 9 cores with each dimension of 460 mm x 25 mm x 4 mm. The dimension of edge shields is 150 mm x 20 mm x 4 mm, covering only the centre edge of the NRC cores. The detail structure of the hybrid NRC and NFR core is shown in Fig. 13. The lamination directions of the core material can be seen from the zoom-in view. The core material is placed directly next to the

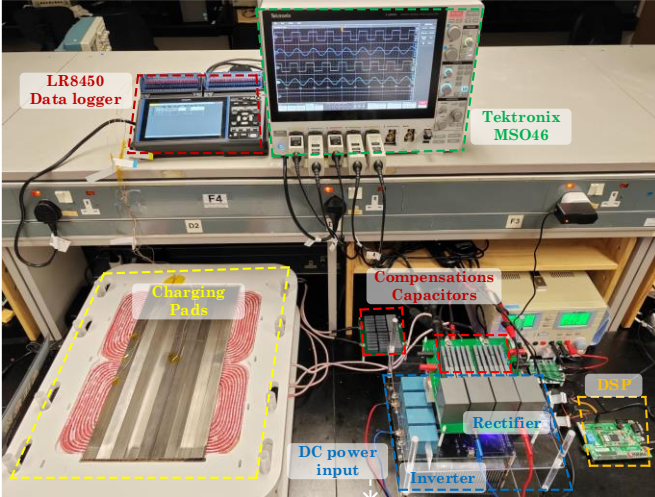


Fig. 12. Hardware prototype of hybrid nanocrystalline core structure for IPT system with high power operation up to 13 kW.

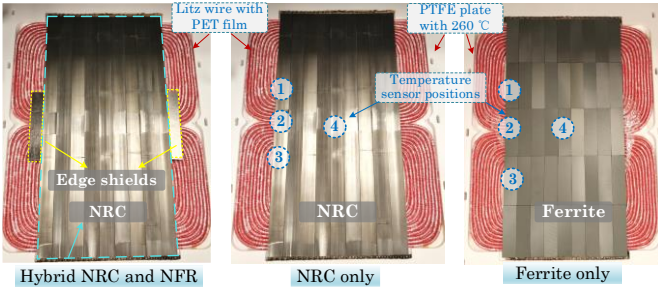


Fig. 13. Different core structures: Hybrid NRC and NFR, NRC only, and Ferrite only for double-D coupler pads.

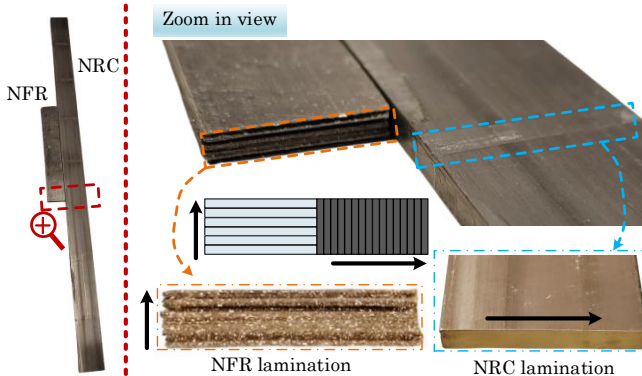


Fig. 14. Hybrid NRC and NFR core on the edge with different lamination directions.

coils. The windings use litz wires with PET film (1×1500 strands, 5.6 mm diameter) to reduce skin and proximity effect.

Four K-type thermal couplers are placed on position 1 to 4. Position 2 is the centre edge of the outer core, which is the position with highest flux density based on previous analysis. Position 1 and 3 are selected for comparison within the centre edge while position 4 is select to compare the inner temperature with the edges.

### C. Passive parameters

System passive parameters with different cores are measured and compared in Table II. Airgap between the primary and

TABLE II PASSIVE PARAMETERS WITH DIFFERENT CORES

Item	DMR44	NRC	Hybrid NRC & Ferrite	Hybrid NRC & NFR
Air gap	145 mm	145 mm	145 mm	145 mm
$L_1$	133.1 $\mu\text{H}$	142 $\mu\text{H}$	142.2 $\mu\text{H}$	142.9 $\mu\text{H}$
$L_2$	133.0 $\mu\text{H}$	141.3 $\mu\text{H}$	141.4 $\mu\text{H}$	142.1 $\mu\text{H}$
$M$	28.8 $\mu\text{H}$	34.7 $\mu\text{H}$	34.8 $\mu\text{H}$	35.3 $\mu\text{H}$
$k$	0.216	0.245	0.245	0.249
$C_1$	26.4 nF	24.75 nF	24.75 nF	24.75 nF
$C_2$	26.4 nF	24.75 nF	24.75 nF	24.75 nF
$f_{res1}$	84.90 kHz	84.90 kHz	84.84 kHz	84.63 kHz
$f_{res2}$	84.94 kHz	85.11 kHz	85.08 kHz	84.87 kHz

secondary pad is 145 mm. Overall, all NRC cores show superior passive parameters compared with ferrite DMR44, while the most promising parameters are measured in hybrid NRC & NFR cores. The improved self inductances, mutual inductances and coupling coefficients allow possibility for higher efficiency according to (4).

Considering hybrid cores, the implementation of edge shielding presents varying results depending on the materials used. The ferrite edge shield doesn't demonstrate a noticeable alteration in the passive parameters, suggesting its shielding is less effective due to its low permeability and solid structure. This observation aligns with the deduction made based on the intuitive magnetic circuit model. The target resonant frequency for capacitor compensation is 85 kHz while the actual deviates slightly because of the available standard values of capacitances, as well as the withstanding voltage, maximum current, creepage and clearance distances of the capacitors. Since the inductance of NRC and hybrid NRC cores are similar, the same compensation networks are employed for them. Capacitor banks for ferrite are redesigned to keep different core structures in the same operating point and therefore ensure a fair comparison.

### D. Efficiency and power output

Fig. 14 shows the measured waveforms of the IPT with hybrid NRC & NFR cores in 6.6kW, 8.1kW, 11.1kW and 13.8 kW respectively. The inverter switching frequency is set to be 86.8 kHz, to let the output impedance be slightly inductive and achieve zero voltage switching (ZVS) for the inverter, which can be verified with smooth inverter voltage. The sinusoidal currents and the near zero phase angle (ZPA) between the current and voltage indicating a close-to-resonance operation.

The power output over input voltage and efficiency over output power are measured and shown in Fig. 15. The previously mentioned four distinct core structures are examined, including hybrid NRC-NFR, hybrid NRC-ferrite (FER), standalone NRC, and standalone ferrite DMR44. The output power  $P_{out}$  is proportional to  $U_{DC}^2$ , demonstrated in Fig. 14(a). With higher mutual inductances, the reflected load  $Z_{ref}$  is higher, resulting in lower current with the same input voltage. Thus, the hybrid NRC & NFR core necessitates a higher voltage to attain equivalent output power when compared to other core structures.

The DC-DC efficiency is shown in Fig. 16(b), calculated as (7) with injected power, output current and input DC voltage.

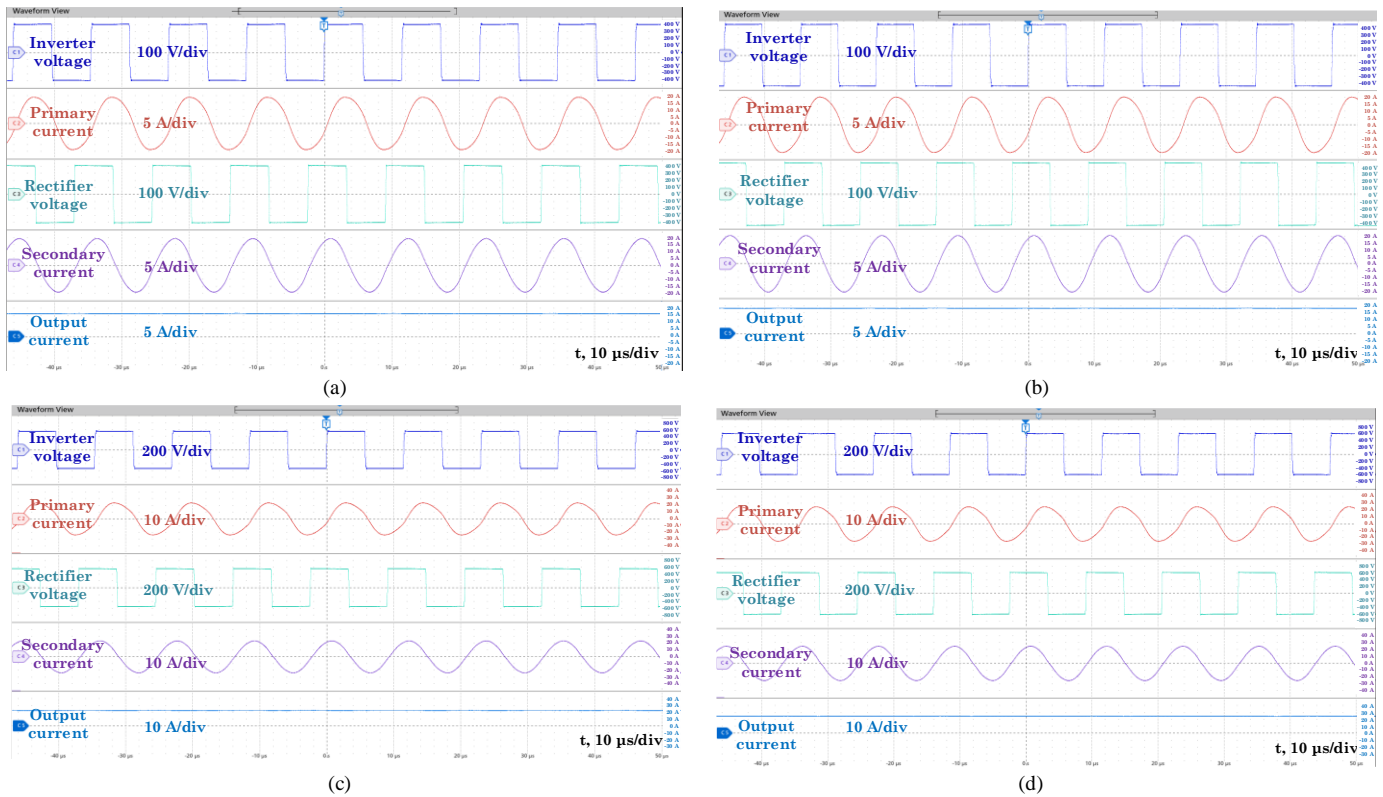


Fig. 15. Measured voltage and current waveforms of the IPT system with hybrid NRC & NFR core when operate at different power levels. (a)  $U_{DC} = 410$  V,  $P_{out} = 6.6$  kW. (b)  $U_{DC} = 480$  V,  $P_{out} = 8.1$  kW. (c)  $U_{DC} = 570$  V,  $P_{out} = 11.1$  kW. (d)  $U_{DC} = 600$  V,  $P_{out} = 13.8$  kW.

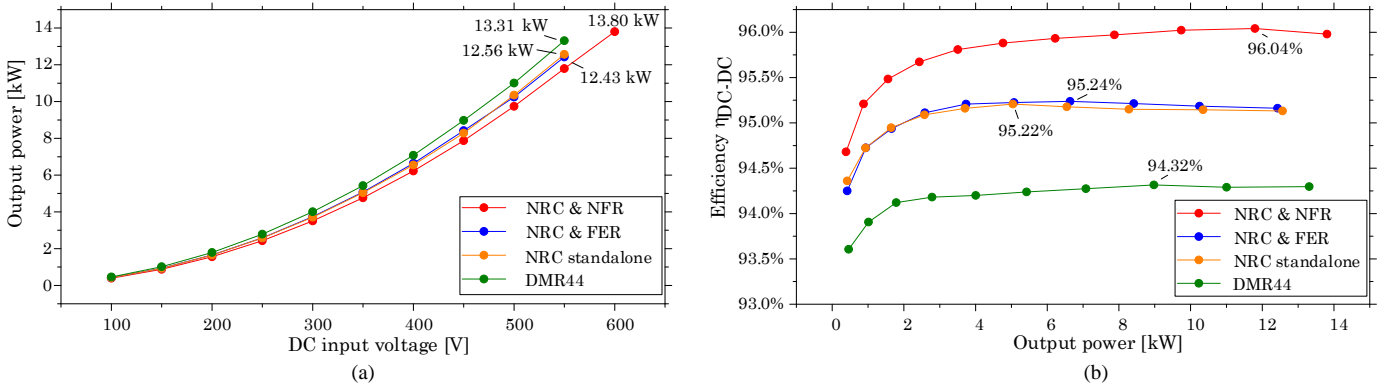


Fig. 16. Experimental comparison of different core structures. (a) Output power over input voltage up to 600V. (b) Efficiency over output power up to 13kW

The measurements were done after 1-minute operation when the injected power stabilized. With hybrid NRC & NFR core, the efficiency improves dramatically, reaching a peak value of 96.04%, which is almost 2% higher than DMR44 under the same output power up to 13 kW. Even at low output power below 1kW, the efficiency maintains above 94.5%.

The NRC and hybrid NRC & FER also demonstrate higher efficiency than ferrite, with 95.22% and 95.24% peak efficiencies respectively. However, this minor difference between them implies a less effective countermeasure against the edge loss with the ferrite edge shields. DMR44 has lowest efficiency among the four core structures with the peak value only at 94.32%.

### E. Initial thermal evaluations

Experiments were then performed to compare the thermal

performances of different core structure. The K-type thermocouples are allocated on previously introduced position 1 to 4, shown in Fig. 12. Initial tests were first performed on nanocrystalline cores for 2 minutes at different power levels with ambient temperature of 22 °C. Fig. 16 shows that the temperature rises at the four positions. It is obvious that the temperature rises at position 1, 2, and 3 (the edge positions) are much higher than position 4 at the centre.

Particularly, when the output power reached over 13 kW, the NRC coupler pad experienced a dramatic temperature increase at the edge after 2 minutes operation, exceeding the resin's melting point of 155 °C. The significant temperature disparity across the layers led to severe mechanical stress on the outer layer of the outer core bar. This was due to the substantial variations in thermal expansions in the different layers, causing

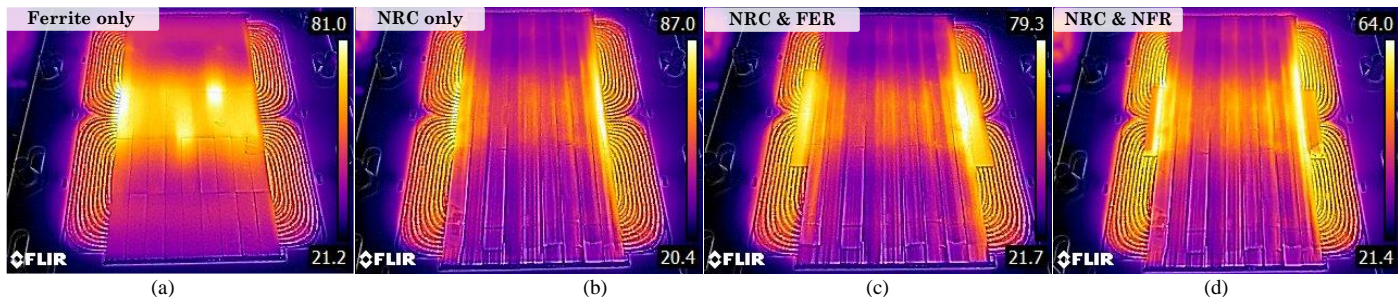


Fig. 18. Thermal images of different core structures after 2-hour operation at continuous 6.6 kW output power. (a) Ferrite DMR44 core only. (b) NRC only. (c) Hybrid NRC & FER structure. (d) Proposed hybrid NRC & NFR structure.

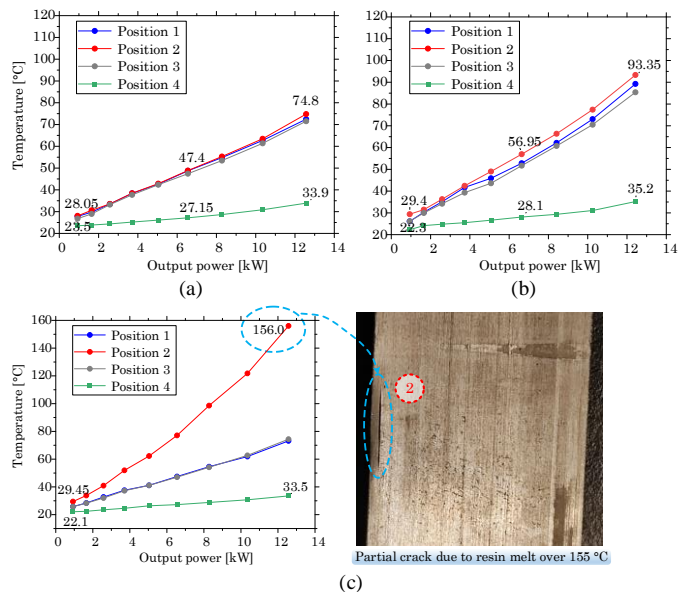


Fig. 17. Temperatures with different core structures. (a) Hybrid NRC & NFR. (b) Hybrid NRC & FER. (c) NRC standalone and core crack at position 2 due to overheating by edge loss.

mechanical damage and the formation of cracks at the edge, as illustrated in Fig. 16(c). This occurrence underscores a significant disadvantage of the laminated core used in double D winding configurations.

With the introduction of the proposed nanocrystalline cores, this failure can be avoided. Hybrid NRC & NFR demonstrates the most promising result by reducing the maximum temperature from 156 °C to 74.8 °C, while the hybrid NRC & FER reduced to 93.35 °C. The results are shown in Fig. 16(a) and Fig. 16(b) respectively.

#### F. Long-duration thermal performance

Long-duration tests were then performed under the condition of 6.6 kW output power, with 2-hours operation time. Fig. 17 shows the results captured by the thermal camera which can interpret the thermal distributions. The highest temperatures of NRC cores were observed at the edge, while the highest temperatures of ferrite were observed in the centre. Micro airgaps between the ferrite core also contribute to generating the hot spots. This highlights the drawback of Mn-Zn ferrite cores using in IPTs, since thin ferrites with a high length-to-width ratio are not commonly available in the market. These

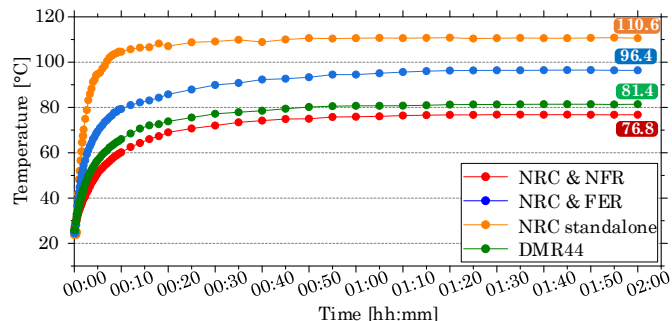


Fig. 19. Measured maximum temperatures of different core structures after 2-hour continuous operation at output power of 6.6 kW

micro airgaps are almost unavoidable given ferrite's geometric properties.

Thermal couples are then used to capture the maximum temperature at the designated positions, shown in Fig. 18. After 2-hour operation, the highest temperature 110.6 °C was observed on the NRC core, which was much higher than the 81.4 °C recorded for ferrite DMR44, despite NRC having higher efficiency. This is attributed to the concentration of core loss at the edge, and the thermal transmission of NRC being constrained by insulating resins with low thermal conductivity. As a result, hot spots were formed along the centre edge of the outer cores with extremely high peak temperatures compared with inner positions. Using the proposed hybrid cores alleviate this situation, resulting a reduced temperature at 96.4 °C with hybrid NRC & FER and 76.8 °C with hybrid NRC & NFR.

Among the four core structures, the proposed hybrid NRC & NFR showed the lowest maximum temperature as well as a more even temperature distribution. Experiments proved that the performance of this hybrid core exceeds traditional ferrite both in efficiency and thermal behaviour in high-power IPT designs.

#### G. Discussion

The effectiveness of NFR shielding for the NRC accredited to the lamination with different orientation as well as the low magnetic reluctance of the material. Even though the overall permeability of NFR is roughly the same as ferrite due to the micro airgaps and adhesive holes inside the ribbon. The high permeable material inside can still effectively redirect the flux entering the edges, and therefore reduces the edge loss. In the meantime, due to the crushed-flake structure, the NFR core does

not experience high eddy current loss even when it is placed in strong excitations. The combination of NRC and NFR then achieves promising efficiency and temperature distribution, benefited from their own strengths. The former one conducts the main flux to increase coupling while the latter one compensates the uneven flux distribution and eddy current loss on the edge. Ferrite edge shielding shows very limited improvement because of the low permeability compared with the permeability of the NRC ribbons. Also, the solid structure does not alter the direction of the flux entering to the NRC edges.

Other methods to mitigate the edge losses like core splitting [15] and [16], core filleting and bevelling [36], and multi material magnetic core [37] require complex manufacturing to modify the mechanical structure of the laminated cores. Considering the much thinner cores than inductors and transformers in IPT applications, modification of mechanical structure could decrease the yield rate and increase the cost greatly in massive production. Additionally, those methods were not analysed for IPT applications, where the airgap is not controllable and leakage flux dominates. This brings intrinsic differences compared with transformer and inductor design because of the non-uniform flux directions. The proposed NFR shielding with different lamination orientation provides a direct and generalized method to reduce edge loss in IPT applications.

## VI. CONCLUSION

This paper explores the characteristic of novel nanocrystalline ribbon materials in high-power IPT applications. An intuitive magnetic model is presented to explain the phenomenon of the edge effect in laminated cores. Countermeasures are proposed accordingly, taking advantage of the high permeability and flexibility of the novel nanocrystalline materials.

Furthermore, a 13-kW 600-V 85-kHz hybrid NRC & NFR based wireless charging platform has been built and tested, where the proposed hybrid nanocrystalline core structure can effectively improve the DC-DC transmission efficiency to 96.04% in contrast to 94.32% with conventional ferrite core configuration. Furthermore, the hybrid core structure demonstrates superior thermal performance characteristics. It maintains a lower operating temperature and ensures a more homogeneous thermal distribution, achieved predominantly through the minimization of core edge loss. This even heat distribution reduces the risk of component failure due to overheating, increasing the overall reliability of the system. The study, therefore, reinforces the viability of nanocrystalline materials in enhancing IPT performance and expands their potential usage in high-power industrial applications.

## REFERENCES

- [1] P. K. Chittoor, B. Chokkalingam, and L. Mihet-Popa, "A Review on UAV Wireless Charging: Fundamentals, Applications, Charging Techniques and Standards", *IEEE Access*, vol. 9, pp. 69235–69266, 2021.
- [2] Z. Zhang, H. Pang, A. Georgiadis, and C. Cecati, "Wireless Power Transfer—An Overview", *IEEE Transactions on Industrial Electronics*, vol. 66, no. 2, pp. 1044–1058, Feb. 2019.
- [3] D. Patil, M. K. McDonough, J. M. Miller, B. Fahimi, and P. T. Balsara, "Wireless Power Transfer for Vehicular Applications: Overview and Challenges", *IEEE Transactions on Transportation Electrification*, vol. 4, no. 1, pp. 3–37, Mar. 2018.
- [4] H. Feng, R. Tavakoli, O. C. Onar, and Z. Pantic, "Advances in High-Power Wireless Charging Systems: Overview and Design Considerations", *IEEE Transactions on Transportation Electrification*, vol. 6, no. 3, pp. 886–919, Sep. 2020.
- [5] A. A. S. Mohamed, A. A. Marim, and O. A. Mohammed, "Magnetic Design Considerations of Bidirectional Inductive Wireless Power Transfer System for EV Applications", *IEEE Transactions on Magnetics*, vol. 53, no. 6, pp. 1–5, Jun. 2017.
- [6] H. Zhao *et al.*, "Comprehensive Investigation on the Influence of Magnetic Materials on the Weight and Performance of Onboard WPT Systems", *IEEE Transactions on Industry Applications*, vol. 58, no. 5, pp. 6842–6851, Sep. 2022.
- [7] H. Zeng, Z. Liu, Y. Hou, T. Hei, and B. Zhou, "Optimization of Magnetic Core Structure for Wireless Charging Coupler", *IEEE Transactions on Magnetics*, vol. 53, no. 6, pp. 1–4, Jun. 2017.
- [8] F. Fiorillo, C. Beatrice, M. Coisson, and L. Zhemchuzhna, "Loss and Permeability Dependence on Temperature in Soft Ferrites", *IEEE Transactions on Magnetics*, vol. 45, no. 10, pp. 4242–4245, Oct. 2009.
- [9] Y. Matsuo, K. Ono, T. Hashimoto, and F. Nakao, "Magnetic properties and mechanical strength of MnZn ferrite", *IEEE Transactions on Magnetics*, vol. 37, no. 4, pp. 2369–2372, Jul. 2001.
- [10] M. Wang, J. Feng, Y. Shi, and M. Shen, "Demagnetization Weakening and Magnetic Field Concentration with Ferrite Core Characterization for Efficient Wireless Power Transfer", *IEEE Transactions on Industrial Electronics*, vol. 66, no. 3, pp. 1842–1851, Mar. 2019.
- [11] S. Kwon, S. Kim, H. Yim, K. H. Kang, and C. S. Yoon, "High saturation magnetic flux density of Novel nanocrystalline core annealed under magnetic field", *Journal of Alloys and Compounds*, vol. 826, p. 154136, 2020.
- [12] W. Zhang, Q. Yang, Y. Li, Z. Lin, M. Yang, and M. Mi, "Comprehensive Analysis of Nanocrystalline Ribbon Cores in High-Power-Density Wireless Power Transfer Pads for Electric Vehicles", *IEEE Transactions on Magnetics*, vol. 58, no. 2, pp. 1–5, Feb. 2022.
- [13] D. E. Gaona, S. Ghosh, and T. Long, "Feasibility Study of Nanocrystalline-Ribbon Cores for Polarized Inductive Power Transfer Pads", *IEEE Transactions on Power Electronics*, vol. 35, no. 7, pp. 6799–6809, Jul. 2020.
- [14] D. E. Gaona, C. Jiang, and T. Long, "Highly efficient 11.1-kW wireless power transfer utilizing nanocrystalline ribbon cores", *IEEE Transactions on Power Electronics*, vol. 36, no. 9, pp. 9955–9969, 2021.
- [15] Y. Wang, G. Calderon-Lopez, and A. J. Forsyth, "High-Frequency Gap Losses in Nanocrystalline Cores", *IEEE Transactions on Power Electronics*, vol. 32, no. 6, pp. 4683–4690, Jun. 2017.
- [16] G. Calderon-Lopez, Y. Wang, and A. J. Forsyth, "Mitigation of Gap Losses in Nanocrystalline Tape-Wound Cores", *IEEE Transactions on Power Electronics*, vol. 34, no. 5, pp. 4656–4664, May 2019.
- [17] M. Xiong, X. Wei, Y. Huang, Z. Luo, and H. Dai, "Research on Novel Flexible High-Saturation Nanocrystalline Cores for Wireless Charging Systems of Electric Vehicles", *IEEE Transactions on Industrial Electronics*, vol. 68, no. 9, pp. 8310–8320, Sep. 2021.
- [18] Z. Luo, X. Li, C. Jiang, and T. Long, "Characterization of Nanocrystalline Flake Ribbon for High Frequency Magnetic Cores", *IEEE Transactions on Power Electronics*, vol. 37, no. 12, pp. 14011–14016, Dec. 2022.
- [19] S. Yin, K. J. Tseng, R. Simanjorang, Y. Liu, and J. Pou, "A 50-kW High-Frequency and High-Efficiency SiC Voltage Source Inverter for More Electric Aircraft", *IEEE Transactions on Industrial Electronics*, vol. 64, no. 11, pp. 9124–9134, Nov. 2017.
- [20] W. Zhang and C. C. Mi, "Compensation Topologies of High-Power Wireless Power Transfer Systems", *IEEE Transactions on Vehicular Technology*, vol. 65, no. 6, pp. 4768–4778, Jun. 2016.
- [21] X. Dai, X. Li, Y. Li, and A. P. Hu, "Maximum Efficiency Tracking for Wireless Power Transfer Systems with Dynamic Coupling Coefficient Estimation", *IEEE Transactions on Power Electronics*, vol. 33, no. 6, pp. 5005–5015, Jun. 2018.

- [22] F. Fiorillo, C. Beatrice, O. Bottauscio, and E. Carmi, "Eddy-Current Losses in Mn-Zn Ferrites", *IEEE Transactions on Magnetics*, vol. 50, no. 1, pp. 1–9, Jan. 2014.
- [23] S. Yamada and E. Otsuki, "Analysis of eddy current loss in Mn-Zn ferrites for power supplies", *IEEE Transactions on Magnetics*, vol. 31, no. 6, pp. 4062–4064, Nov. 1995.
- [24] D. Lin, P. Zhou, W. N. Fu, Z. Badics, and Z. J. Cendes, "A dynamic core loss model for soft ferromagnetic and power ferrite materials in transient finite element analysis", *IEEE Transactions on Magnetics*, vol. 40, no. 2, pp. 1318–1321, Mar. 2004.
- [25] T. Kawano, A. Fujita, and S. Gotoh, "Analysis of power loss at high frequency for MnZn ferrites", *Journal of Applied Physics*, vol. 87, no. 9, pp. 6214–6216, May 2000.
- [26] V. Rybachuk and Y. Kulynych, "Influence of anisotropy on eddy current conductivity measurement", in *2016 IEEE International Conference on Mathematical Methods in Electromagnetic Theory (MMET)*, Jul. 2016.
- [27] M. Markovic and Y. Perriard, "Eddy current power losses in a toroidal laminated core with rectangular cross section", in *2009 International Conference on Electrical Machines and Systems*, Nov. 2009.
- [28] M. C. Kulan, N. J. Baker, K. A. Liogas, O. Davis, and J. Taylor, "Improved Core Loss Calculations in Soft Magnetic Composites Considering 3-D Magnetic Flux Density Vectors and Geometry Dependent Eddy Currents", in *2023 IEEE International Electric Machines & Drives Conference (IEMDC)*, May 2023.
- [29] J. Reinert, A. Brockmeyer, and R. W. A. A. De Doncker, "Calculation of losses in ferro- and ferrimagnetic materials based on the modified Steinmetz equation", *IEEE Transactions on Industry Applications*, vol. 37, no. 4, pp. 1055–1061, Jul. 2001.
- [30] J. Muhlethaler, J. Biela, J. W. Kolar, and A. Ecklebe, "Improved Core-Loss Calculation for Magnetic Components Employed in Power Electronic Systems", *IEEE Transactions on Power Electronics*, vol. 27, no. 2, pp. 964–973, Feb. 2012.
- [31] H. Kaimori, A. Kameari, and K. Fujiwara, "FEM Computation of Magnetic Field and Iron Loss in Laminated Iron Core Using Homogenization Method", *IEEE Transactions on Magnetics*, vol. 43, no. 4, pp. 1405–1408, Apr. 2007.
- [32] K. Preis, O. Biro, and I. Ticar, "FEM analysis of eddy current losses in nonlinear laminated iron cores", *IEEE Transactions on Magnetics*, vol. 41, no. 5, pp. 1412–1415, May 2005.
- [33] K. Hollaus and M. Schöbinger, "A Mixed Multiscale FEM for the Eddy-Current Problem With  $T$ ,  $\Phi$ - $\Phi$  in Laminated Conducting Media", *IEEE Transactions on Magnetics*, vol. 56, no. 4, pp. 1–4, Apr. 2020.
- [34] "Nanocrystalline Soft Magnetic Material FINEMET® | Proterial, Ltd." [https://www.proterial.com/e/products/elec/tel/p02\\_21.html](https://www.proterial.com/e/products/elec/tel/p02_21.html) (accessed Apr. 17, 2023).
- [35] K. Twarowski, M. Kuźmiński, A. Ślowska-Waniewska, H. K. Lachowicz, and G. Herzer, "Magnetostriction of Fe<sub>73.5</sub>Cu<sub>1</sub>Nb<sub>3</sub>Si<sub>15.5</sub>B<sub>7</sub> nanocrystalline alloy", *Journal of Magnetism and Magnetic Materials*, vol. 140–144, pp. 449–450, Feb. 1995.
- [36] T. Tera, H. Taki, and T. Shimizu, "Loss reduction of laminated core inductor used in on-board charger for EVs", in *2014 International Power Electronics Conference (IPEC-Hiroshima 2014 - ECCE ASIA)*, May 2014.
- [37] S. Saha, N. Fernando, and L. Meegahapola, "Multi magnetic material laminated cores: Concept and modelling", in *2017 20th International Conference on Electrical Machines and Systems (ICEMS)*, Aug. 2017.



**Yibo Wang** (Student Member, IEEE) received the B.Eng degree in automation from Nankai University, Tianjin, China, in 2016, and the M.Sc. degree in electrical power engineering from RWTH Aachen University, Aachen, Germany, in 2019. He was a hardware development engineer with Delta Energy Systems (Germany) GmbH from 2019 to 2022. He is currently pursuing his Ph.D degree in the Department of Electrical and Electronics Engineering, The City University of Hong Kong, Hong Kong. His research interests include wireless power transfer technology, power electronics and magnetics design.



**C. Q. Jiang** received the B.Eng. and M.Eng. degrees (First Class Honours) in Electrical Engineering and Automation from Wuhan University, Wuhan, China, in 2012 and 2015, respectively, and the Ph.D. degree in Electrical and Electronic Engineering from The University of Hong Kong, Hong Kong SAR, China, in 2019.

He is currently an Assistant Professor with the Department of Electrical Engineering, City University of Hong Kong, Hong Kong SAR. In 2019, he was a Visiting Researcher at the Nanyang Technological University, Singapore. He was a Postdoctoral Research Associate at the University of Cambridge, U.K. Also, he is affiliated with Clare Hall Cambridge since 2021.



**Chen Chen** received the B.Eng. and M.Eng. degrees in Mechanical Manufacture and Automation from Wuhan University of Technology, Wuhan, China, in 2019 and 2022, respectively.

He is currently pursuing his Ph.D. degree in the department of Electrical and Electronic Engineering, The City University of Hong Kong, Hong Kong. His research interests include wireless power transfer techniques, electric machines, and devices.



**Tianlu Ma** received the B.Eng. degree in College of Instrumentation and Electrical Engineering from Jilin University, China, in 2018, and the M.Sc. degree in School of Electrical Engineering from Xi'an Jiaotong University, China, in 2021. He is currently working toward the Ph.D. degree in the Department of Electrical Engineering, City University of Hong Kong, Hong Kong. His research interests include wireless power transfer modeling and control.



**Xinru Li** (Student Member, IEEE) received the B.Eng. degree in materials science and engineering from the University of Science and Technology Beijing, Beijing, China, in 2017, and the M.Phil. degree in electrical engineering in 2019 from the University of Cambridge, Cambridge, U.K., where he is currently working toward the Ph.D. degree.

His research focuses on magnetic materials, particularly for power electronics applications, wireless charging systems, and high-frequency transformers.



**Teng Long** (Member, IEEE) received the B.Eng. degree from the Huazhong University of Science and Technology, Wuhan, China, the first class B.Eng. (Hons.) degree from the University of Birmingham, Birmingham, U.K., in 2009, and the Ph.D. degree from the University of Cambridge, Cambridge, U.K., in 2013.

Until 2016, he was a Power Electronics Engineer with the General Electric (GE) Power Conversion business, Rugby, U.K.. He is currently a Full Professor with the University of Cambridge. His research interests include power electronics, electrical machines, and machine drives.

Dr. Long is a Chartered Engineer (C.Eng.) registered with the Engineering Council in the U.K.